Journal of Materials Chemistry C

ROYAL SOCIETY OF CHEMISTRY

PAPER

View Article Online
View Journal

Cite this: DOI: 10.1039/d5tc04343c

Ultrafast response UV-regulated graphene-based NO_2 gas sensor

Wei Jin,[a] Cao Tang,[a] Hongyuan Zhao,[a] Xue Xiao,[a] Xin Qi,[a] Xiangting Zhang,[a] Hafiza Sana Haider,[a] Jianxiong Zhao,[abc] Yanqing Ma *[abcd] and Lei Ma *[abc]

Received 11th December 2025,
Accepted 28th February 2026

DOI: 10.1039/d5tc04343c

rsc.li/materials-c

In this study, we developed a UV-regulated graphene-based NO_2 gas sensor using high-quality graphene synthesized *via* chemical vapor deposition (CVD) and fabricated through micro-nano processing techniques. To explore the fundamental sensing mechanism, we conducted measurements under high-purity nitrogen conditions, which revealed that UV illumination raises the Fermi level of graphene, thereby enhancing the adsorption energy and enabling ultrafast NO_2 response. By combining a simple kinetic model with density functional theory (DFT)-calculated adsorption energies for differently doped graphene, we quantitatively link the adsorption energy to the relaxation time and thereby rationalize how UV-induced Fermi-level modulation accelerates the NO_2 adsorption–desorption dynamics. Building upon this mechanistic insight, we further validated the sensor's performance under laboratory air conditions. The sensor demonstrated a rapid room-temperature response to NO_2 over the concentrations range of 0.1–5 ppm, with response times below 5 s, and achieved a 1 s response time at 100 ppb. It also exhibited excellent stability, maintaining consistent responsivity over 638 days and during 100 consecutive tests, with reliable operation under relative humidity (RH) levels up to 75%. Moreover, selectivity tests showed a pronounced response to NO_2 and negligible responses to various common interfering gases even at much higher concentrations. These results highlight the sensor's potential for practical, real-time NO_2 monitoring and offer a new approach for achieving fast gas detection through optoelectronic modulation of graphene.

1. Introduction

NO_2 is a major air pollutant that significantly impacts human health and the environment. Exposure to NO_2 can lead to respiratory problems, cardiovascular diseases, and other adverse health effects. Additionally, NO_2 contributes to the formation of acid rain and smog, which have detrimental effects on ecosystems and infrastructure. Therefore, monitoring NO_2 concentrations is of paramount importance for environmental protection and public health. A wide range of NO_2 sensing principles has been developed and commercialized, including electrochemical sensors, optical methods, and chemiresistive devices. Benefiting from their simple structure, low cost, and compatibility with miniaturized integrated electronics, chemiresistive sensors based on semiconducting metal oxides such as SnO_2 have therefore become one of the most widely adopted platforms for solid-state NO_2 detection.[1,2] These materials have been extensively studied and applied due to their high sensitivity and technological maturity. However, these sensors typically require high operating temperatures, often exceeding 200 °C, to achieve optimal performance. This requirement results in increased energy consumption and limits their applicability in certain environments, such as portable or low-power devices. Moreover, high-temperature operation can also lead to issues such as sensor drift and reduced lifespan, further complicating their practical deployment.[3]

To address these challenges, there is a growing need for the development of NO_2 sensors that operate at room temperature or near-room temperature, while maintaining high sensitivity and selectivity. Recent advances in materials science and nanotechnology have opened new possibilities for the design and fabrication of such sensors. Graphene, as a single-atom-thick material, exhibits outstanding properties such as a large specific surface area, excellent electrical conductivity, and low electronic noise.[4] Building on these advantages, in 2007, Geim and colleagues first demonstrated the gas-sensing capabilities of mechanically exfoliated graphene for NO_2, NH_3, and

[a] Tianjin International Center for Nanoparticles and Nanosystems, Tianjin University, Tianjin, 300072, P. R. China. E-mail: lei.ma@tju.edu.cn, mayanqing@tju.edu.cn
[b] Tianjin Key Laboratory of Low-dimensional Electronic Materials and Advanced Instrumentation, Tianjin, 300072, P. R. China
[c] Haihe laboratory for Low-dimensional Electronic Materials, Add 1 to No. 57 Wujiayao street, Hexi District, Tianjin, 300074, P. R. China
[d] School of Precision Instrument and Opto-electronics Engineering, Tianjin University, Tianjin, 300072, P. R. China

H_2O, laying the foundation for graphene-based gas sensors.[5] Since then, various graphene materials have been explored for gas sensing, including mechanically exfoliated graphene,[6–9] epitaxial graphene on silicon carbide (SiC),[10–15] reduced graphene oxide (RGO),[16–22] and CVD graphene.[23–27] Among these, CVD graphene stands out due to its relatively low production cost, scalability for high-quality synthesis, and excellent compatibility with modern semiconductor processing techniques.[28]

Despite substantial progress, graphene-based NO_2 sensors still suffer from lengthy response times, which severely limit their applicability in real-time monitoring scenarios.[24,25,29–31] Most graphene-based NO_2 sensors exhibit response times exceeding 100 s.[24,26,27,30–36] Notable exceptions include sensors modified with sulfonated RGO or nanoparticles such as Ag and SnO_2,[37–39] which achieve response times below 40 s. Other approaches, such as dual modification with Pd and SnO_2 nanoparticles or polypyrrole deposition on CVD graphene,[40,41] have reported response times as low as 2 s. However, these methods often involve complex chemical functionalization, multilayer hybrid structures, or additional heating elements, which increase fabrication complexity and hinder large-scale integration and practical deployment.

In this study, we present a UV-regulated CVD graphene-based gas sensor capable of achieving ultrafast NO_2 detection at room temperature. Unlike most previously reported graphene-based NO_2 sensors that rely on intensive chemical functionalization or hybrid nanostructures to accelerate the response, our sensor uses pristine, high-purity monolayer CVD graphene as the sensing channel and exploits UV illumination as an external knob to tune the Fermi level and response kinetics. Under high-purity nitrogen, we first demonstrate that UV illumination can dynamically modulate the Fermi level of the CVD graphene channel and thereby accelerate the NO_2 response in a controllable manner, and we rationalize the observed UV-power-dependent response behavior with a simple kinetic model. Furthermore, we show that this UV-regulated mechanism remains effective in laboratory air with up to 75% relative humidity, where the sensor achieves a 1 s response at 100 ppb NO_2, maintains excellent long-term stability over 638 days, and exhibits high selectivity against interfering gases, highlighting UV-driven Fermi-level engineering of high-quality CVD graphene as a feasible route toward fast-response NO_2 sensing under realistic operating conditions.

2. Experimental

2.1. Graphene growth

Graphene was synthesized using chemical vapor deposition to achieve high quality and minimal defects. Initially, copper foil with a thickness of 25 μm was pre-treated with hydrochloric acid to remove surface oxides, ensuring a clean and smooth surface. The cleaned copper foil was then placed in a quartz tube and annealed at 1080 °C in an argon-hydrogen atmosphere (10 : 1 by volume) for 1–2 hours, as a standard pretreatment in CVD graphene growth that promotes surface recrystallization and grain growth of Cu, thereby facilitating the formation of uniform monolayer graphene films.[42,43] Following this, graphene growth was carried out at the same temperature of 1080 °C under a gas mixture of argon, methane, and hydrogen (200 : 1 : 20 by volume) for 10 minutes. This process successfully yielded high-quality graphene films.

2.2. Sensor fabrication

Bottom-gated graphene field-effect transistors (GFETs) were fabricated on Si/SiO_2 substrates. Initially, photolithography combined with electron beam deposition was employed to define the gate and source/drain electrodes (Cr 20 nm/Au 10 nm) on the substrate. Subsequently, photolithography and atomic layer deposition (ALD) techniques were used to deposit a 15 nm thick aluminum oxide dielectric layer over the gate electrode.

After completing the substrate preparation, wet transfer techniques were used to transfer CVD-grown graphene onto the pre-patterned substrate with electrodes and the dielectric layer. The transferred graphene was then patterned into channel structures with dimensions of 20 μm × 20 μm using photolithography and reactive ion etching (RIE). Finally, silver paste and aluminum wires (30 μm in diameter) were used to connect the fabricated GFET devices to a printed circuit board (PCB) testing platform, completing the assembly of the graphene-based gas sensor.

2.3. Characterization

The structural quality and properties of graphene in the channel region after device fabrication were characterized using a confocal Raman spectrometer (RTS-2) with a laser wavelength of 532 nm. Additionally, the morphological structure of the entire device was examined using scanning electron microscopy (SU3500) and an optical microscope (WY-2000M).

2.4. Testing methods

The gas-sensing test system is depicted in Fig. 1a. The sealed test chamber has an internal volume of 380 mL, and the total gas flow rate was maintained at 1000 sccm for all measurements. NO_2 was supplied from a certified standard gas cylinder with a nominal concentration of 100 ppm NO_2 (balanced in N_2) and was diluted by mixing with the base gas to obtain the desired test concentrations. Two types of base gases were used in this study: high-purity nitrogen (99.999%) and laboratory air. Nitrogen was selected to isolate the intrinsic interaction between graphene and NO_2, serving the purpose of mechanism exploration. Air was used to evaluate the sensor's practical performance under realistic conditions. In the following, the gas mixture without NO_2 is referred to as the base gas, and the mixture containing NO_2 is referred to as the target gas.

When ball valve 1 and ball valve 3 were opened, the base gas for testing was high-purity nitrogen (99.999%, nominally 0% relative humidity). When ball valve 2 and ball valve 4 were opened, the base gas for testing was air. For 0% relative humidity, dry air was generated by mixing pure nitrogen and

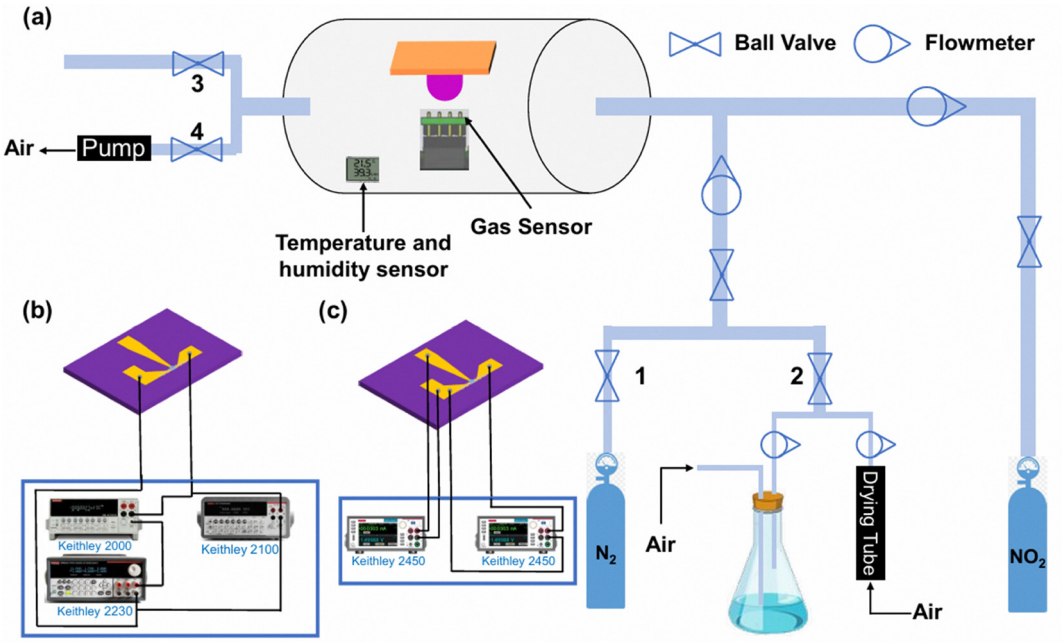

Fig. 1 (a) Schematic diagram of the gas response testing setup. (b) Gas response testing method and (c) Transfer characteristic testing method.

oxygen at a flow-rate ratio of 79 : 21 using calibrated rotameter flow meters, so that the overall N_2:O_2 composition matches that of ambient air while eliminating water vapor. For measurements at non-zero humidity, part of the air stream was passed through a water bubbler at room temperature and then mixed with the dry air stream, and the flow-rate ratio between the dry and humidified branches was adjusted by rotameter flow meters to obtain the desired relative humidity. The relative humidity inside the chamber (0–75% RH) was monitored *in situ* by a commercial hygrometer and allowed to stabilize before each measurement.

A Keithley 2230 power supply was used to apply a constant voltage across the sensor terminals. Simultaneously, a Keithley 2100 multimeter and a Keithley 2000 multimeter were employed to measure the voltage drop across the sensor and the current through the circuit, respectively (test setup illustrated in Fig. 1b). From these measurements, the time-dependent resistance of the sensor could be determined.

The transfer characteristics of the sensor were evaluated using two Keithley 2450 source meters. One source meter was configured to apply a gate voltage between the gate and source terminals, while the other applied a fixed drain-source voltage and simultaneously measured the resulting drain current. By incrementally scanning the gate voltage and recording the corresponding changes in drain current, the transfer characteristic curve of the sensor was obtained. A schematic of this test setup is shown in Fig. 1c.

The temperature inside the test chamber was in the range of 20–22 °C during all measurements, corresponding to the ambient laboratory conditions.

UV illumination was provided by a UV LED source (Yonglin Optoelectronics, China). The emission spectrum, measured with a spectrometer, was centered at approximately 265 nm with a full width at half maximum (FWHM) of about 13 nm. The optical output of the LED was adjusted by changing the value of the series resistor in the LED driving circuit, thereby controlling the LED current. The optical power density (OPD) at the sensor surface was measured using a high-intensity optical power meter (CEL-NP2000-10, CEAULICHT, China), which directly reports OPD in units of mW cm^{-2}. During the OPD measurements, the distance between the LED and the power-meter probe was kept identical to the distance between the LED and the sensor surface in the gas-sensing tests, so that the reported OPD corresponds to the optical power density incident on the graphene channel.

2.5. Performance metrics

Responsivity (R_e): the responsivity is defined as $R_e = \frac{R_g - R_0}{R_0} \times 100\%$, where R_g is the resistance corresponding to the maximum resistance change after exposure to the target gas and R_0 is the initial resistance in the base gas. In some figures, we plot the absolute responsivity $|R_e|$ to highlight the dependence of the response magnitude on NO_2 concentration.

Response time (R_T): the response time is defined as the time required for the resistance of the sensor to reach 60% of its maximum change after exposure to the target gas within the fixed gas-exposure interval.

In this study, the responsivity R_e and response time R_T defined above were evaluated under two base-gas conditions, namely high-purity nitrogen and laboratory air.

The chemicals and gases used in the experiment, including their CAS numbers, purities, and suppliers, are summarized in Table S1 in the SI.

3. Results and discussion

3.1. Device structure and material characterization

Fig. 2 demonstrates the physical appearance, fabrication process, core structure, microfabrication precision, and material properties of the CVD graphene-based gas sensor. Fig. 2a presents a photograph of the CVD graphene gas sensor mounted on a PCB, showcasing its physical appearance. Fig. 2b schematically illustrates the fabrication process of the CVD graphene GFET device, highlighting the micro-nano fabrication techniques employed. Fig. 2c shows an optical microscope image of the core device structure, revealing the arrangement of the source, gate, and drain electrodes. The central rectangular blue area represents the aluminum oxide dielectric layer, which functions as an insulating layer. Above this layer lies the sensing channel, measuring 20 μm × 20 μm, which serves as the active region for gas molecule adsorption and electron transport. Fig. 2d displays a SEM image of the core device structure, demonstrating the structural integrity and high precision achieved through the microfabrication process. Raman spectroscopy was performed on the region indicated by the white box, with the results presented in Fig. 2e. The Raman spectrum reveals three distinct characteristic peaks at 1342 cm^{-1}, 1581 cm^{-1}, and 2689 cm^{-1}, corresponding to the D, G, and 2D bands of graphene, respectively.[44] Notably, the 2D peak intensity is relatively high, with an intensity ratio of I_{2D}/I_G = 4.66 and the full width at half maximum (FWHM) of the 2D peak is 27.43 cm^{-1}. The ratio of the D peak to the G peak intensity is I_D/I_G = 0.23, indicating that the graphene in the channel is single-layered,[45] with few defects, confirming it as high-quality monolayer graphene.[44–46] To check the uniformity across the whole channel, we also performed Raman measurements on the graphene region on the left-hand side of the gate and the spectrum is presented in Fig. S1. This spectrum shows Raman features and intensity ratios similar to those in Fig. 2e, demonstrating that the graphene on both sides of the channel is high-quality monolayer graphene. In the very narrow central part directly above the bottom-gate metal electrode, a strong fluorescence background originating from the underlying metal makes it difficult to clearly resolve the graphene peaks. However, optical microscopy image (Fig. 2c) shows a uniform color over the entire channel region without any obvious contrast variation, indicating that the whole channel is covered by monolayer graphene.

Unless otherwise specified, each data set (figure or subfigure) was obtained from a single representative sensor, and different data sets may correspond to different but nominally identical sensors. Similar trends were observed across multiple sensors, so slight differences in the absolute responsivity from one data set to another are attributed to device-to-device variation, and our analysis focuses on the relative trends under each set of conditions.

3.2. Electrical and optoelectronic properties under N_2

Fig. 3 illustrates the electrical and optoelectronic properties of the graphene-based gas sensor. All measurements in Fig. 3 were

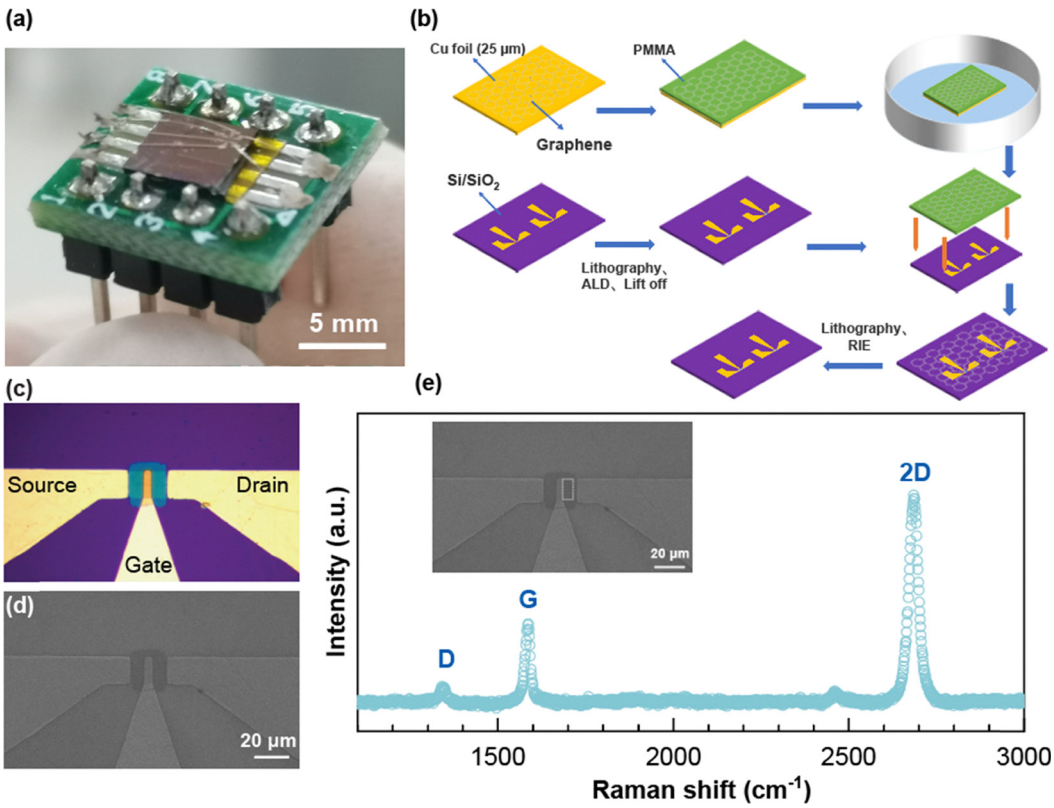

Fig. 2 (a) Photograph of the graphene-based NO_2 sensor. (b) Fabrication process flow of the core GFET device in the sensor. (c) Optical microscopy image and (d) SEM image of the core device structure. (e) Raman spectrum of graphene channel.

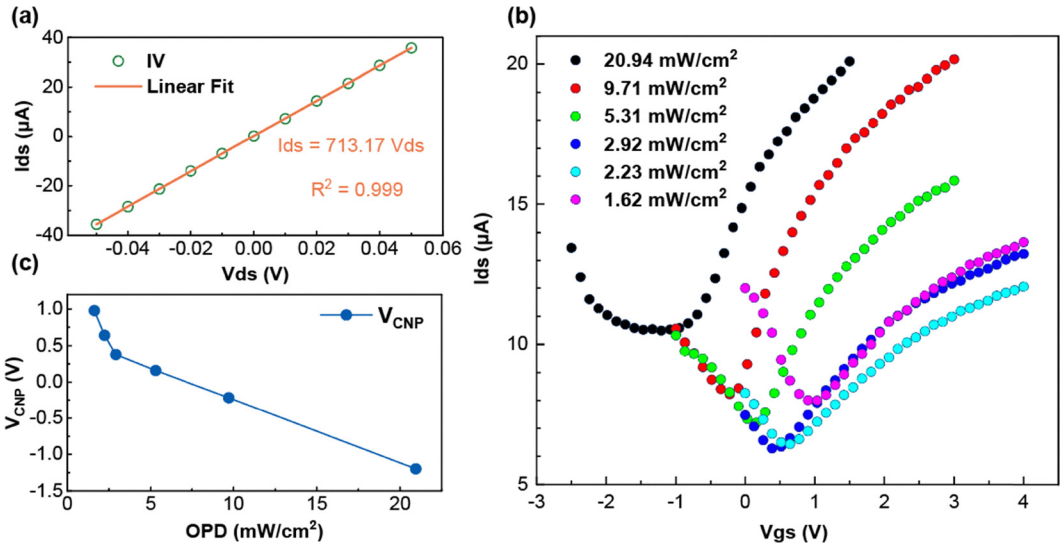

Fig. 3 (a) IV curve of the graphene-based gas sensor without UV. (b) Transfer characteristic curves of the graphene-based gas sensor under different UV power densities and (c) corresponding charge neutrality point (Dirac point).

conducted in high-purity nitrogen at 20–22 °C to exclude interference from ambient oxygen and moisture, allowing a clearer investigation of UV-induced doping effects in graphene. Fig. 3a shows the *I–V* curve of the sensor, revealing a linear relationship between current and voltage with a slope of 713 μA V^{-1} and a fitting coefficient R^2 = 0.99. This linearity indicates ohmic contact between graphene and the electrodes, ensuring efficient charge carrier transport between the graphene sensing layer and the metal electrodes, which is crucial for the stable performance of the sensor. Building on this electrical contact characteristic, we further investigate the optoelectronic response of the device under optical modulation. Fig. 3b presents the transfer characteristic curves of the sensor under different UV power densities. Upon UV illumination, the transfer characteristic curves of graphene shift in the negative gate voltage direction with increasing UV power density. At low UV power densities, graphene exhibits p-type conduction (neutrality point located in the positive gate voltage region). As the UV power density increases, the neutrality point crosses zero gate voltage, transitioning to n-type conduction (neutrality point located in the negative gate voltage region).[47] The UV-induced polarity tuning in graphene can be attributed to photo-assisted surface cleaning and the associated electronic modulation. UV light effectively cleans the graphene surface, promoting the desorption of small molecules such as water and oxygen.[48,49] The desorption of these molecules not only reduces the hole concentration in graphene, weakening the p-type doping effect, but also enables a transition from p-type to n-type conduction under the influence of substrate-induced electron doping in CVD graphene.[50–52] Furthermore, studies by Yow-Jon Lin *et al.* using Kelvin probe force microscopy (KPFM) have shown that UV illumination reduces the work function of graphene, leading to an elevated Fermi level.[53] This behavior is further illustrated in Fig. 3c, which shows the corresponding positions of the graphene charge neutrality point (Dirac point) under different UV power densities. These combined mechanisms demonstrate that UV illumination can effectively raise the Fermi level of graphene, thereby modulating its electronic structure and doping characteristics.

3.3. Ultrafast NO_2 sensing mechanism regulated by UV illumination under N_2

Fig. 4 presents the intrinsic gas-sensing behavior of the graphene-based sensor toward NO_2. Similar to Fig. 3, these tests (Fig. 4) were performed in a high-purity nitrogen environment at 20–22 °C, aiming to further examine the intrinsic adsorption behavior between graphene and NO_2. Fig. 4a shows a schematic of NO_2 molecules adsorbed on the graphene surface, the white spheres represent carbon atoms in graphene, arranged in a typical hexagonal honeycomb structure, while the blue and red spheres represent the nitrogen and oxygen atoms in the NO_2 molecule, respectively. When NO_2 adsorbs onto graphene, electrons transfer from the graphene to the NO_2 molecules, thereby altering the conductivity of graphene. Based on this electron transfer mechanism, Fig. 4b shows the dynamic response curves of the sensor for 100 ppb, 200 ppb, 400 ppb, 2 ppm, and 5 ppm NO_2, measured using the test system in Fig. 1a. The pink-shaded areas represent the response phase during NO_2 exposure. NO_2 was introduced for 100 s and then stopped. From Fig. 4b, it can be seen that, for NO_2 concentrations from 100 ppb to 2 ppm, the sensor resistance increases during NO_2 exposure and the magnitude of the resistance change becomes larger as the NO_2 concentration increases. However, at 5 ppm, the shape of the response curve changes: the resistance first increases and then gradually decreases. This phenomenon can be attributed to the strong electron-withdrawing ability of NO_2 molecules. As the number of adsorbed molecules increases, the graphene transitions from n-type to p-type conductivity, leading to an increase in hole concentration, which ultimately causes a decrease in

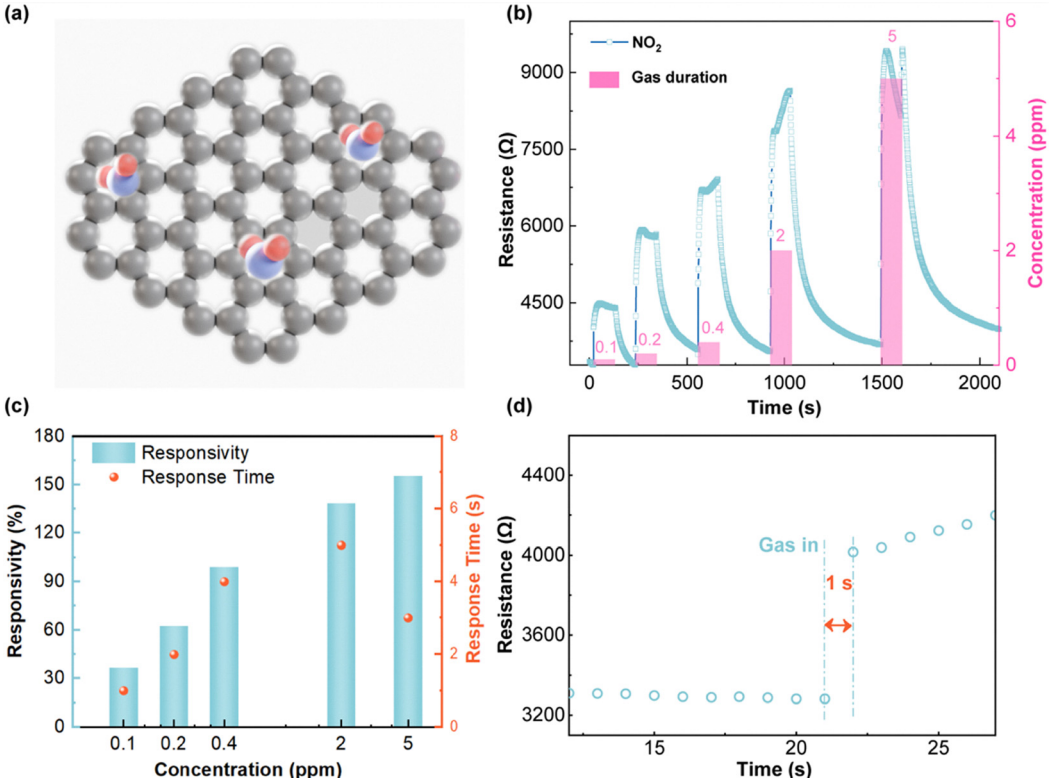

Fig. 4 (a) Schematic of NO_2 molecule adsorption on graphene. (b) Real-time response curves of the graphene-based sensor toward 0.1–5 ppm NO_2. (c) Corresponding responsivity and response time of the sensor as a function of NO_2 concentration. (d) Dynamic response curve of the sensor to 100 ppb NO_2. All measurements were carried out under UV illumination with an optical power density of 89.85 mW cm^{-2} in high-purity nitrogen at 20–22 °C.

resistance.[15,47] This indicates that at high NO_2 concentrations, the electrical properties of graphene undergo complex changes due to the shift in carrier type. The data in Fig. 4b are further summarized in Fig. 4c, which displays the responsivity and response time of the sensor at different NO_2 concentrations. The responsivity increases with NO_2 concentration and tends to saturate at high concentrations, consistent with the n-to-p transition mechanism discussed above. On the other hand, the response time remains below 5 s across all concentrations, demonstrating the rapid response capability of the sensor. To highlight the unique advantage of the sensor in low-concentration regimes, Fig. 4d shows the dynamic response curve of the sensor to 100 ppb NO_2. The response time is only 1 s, showcasing the ultrafast response speed of the sensor.

Fig. 5 illustrates the sensor response under different UV power densities to further elucidate the mechanism behind its

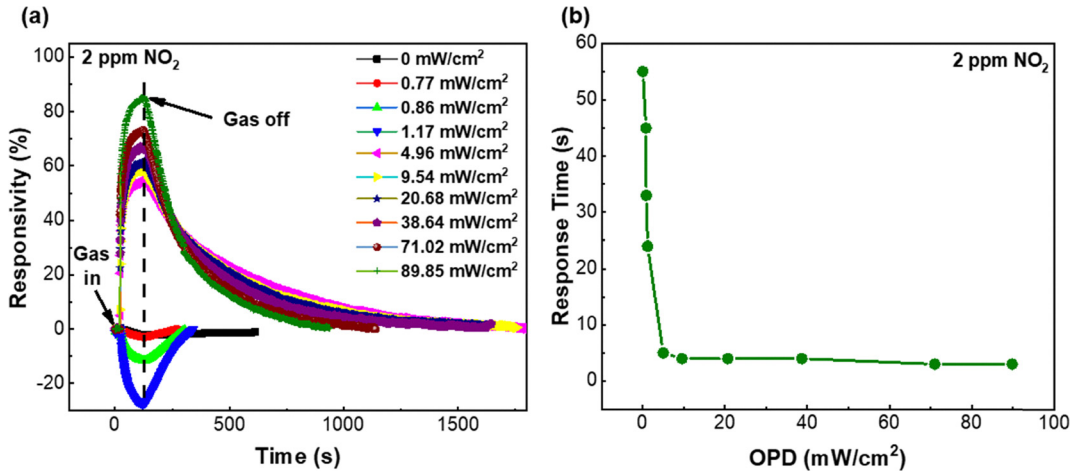

Fig. 5 (a) Dynamic response curves of the graphene-based sensor toward 2 ppm NO_2 under different UV power densities. (b) Corresponding response time of the sensor as a function of UV power density for 2 ppm NO_2. All measurements were conducted in high-purity nitrogen at 20–22 °C.

ultrafast behavior. These experiments were also carried out in high-purity nitrogen at 20–22 °C. Fig. 5a shows the response curves of the sensor at various UV power densities. In the absence of UV illumination (0 mW cm^{-2}), the sensor exhibits a negative response upon exposure to NO_2, that is, the resistance decreases relative to its initial value. This indicates that the graphene channel behaves as p-type, with holes as the majority carriers, and the response amplitude is relatively small. After the gas is turned off, the resistance can gradually recover to the initial value, but the recovery process is noticeably slow. This suggests that, without UV assistance, the desorption kinetics of NO_2 molecules on the graphene surface are sluggish and only a limited number of adsorption–desorption sites can participate in a reversible process.

When the UV power density is increased to 0.77–1.17 mW cm^{-2}, the response amplitude gradually increases and the reversibility becomes more pronounced, indicating that UV illumination begins to effectively modulate the adsorption–desorption process of NO_2. As the UV power density is further increased ($\geq$4.96 mW cm^{-2}), the sensor exhibits a monotonic increase in resistance upon NO_2 introduction, corresponding to a positive responsivity. This behavior indicates that the graphene has converted to n-type conduction, with the Fermi level shifted above the Dirac point and the number of conduction-band electrons sufficient to satisfy the charge-transfer demand of NO_2 molecules. With further increase in UV power density, the responsivity to NO_2 is markedly enhanced and gradually approaches saturation. These phenomena collectively demonstrate that UV illumination plays a crucial role in regulating the gas-sensing behavior by tuning the Fermi level of graphene.

The data in Fig. 5a also reveal the dependence of the response time on UV power density, as summarized in Fig. 5b. As the UV power density increases, the response time decreases significantly from several tens of seconds without illumination to 5 s at 4.96 mW cm^{-2}, and then further shortens and stabilizes on a plateau of 3 s at higher power densities. This indicates that UV illumination greatly accelerates the adsorption and desorption processes of NO_2. Such behavior can be attributed to the UV-induced upward shift of the Fermi level, which increases the effective adsorption energy of NO_2 on the graphene surface and enables the sensor to reach a new equilibrium state within a shorter time.

It should be noted that 89.85 mW cm^{-2} is the maximum stable UV power density provided by the lamp used in our experiments. Under this condition, both the responsivity and the response time of the sensor are close to their optimum and essentially saturated. Therefore, in the performance evaluations conducted in nitrogen and in air, we chose this power density as the operating UV power for the sensor.

To further validate this mechanism, we developed a theoretical model to explain the relationship between adsorption energy, relaxation time, and n-type doping concentration, with the model construction process outlined in the SI and Fig. S2. Fig. 6a illustrates the trend between adsorption energy and relaxation time. As the adsorption energy increases, the relaxation time decreases, indicating that with higher adsorption energy, the time required for gas molecules to adsorb and reach saturation on the graphene surface decreases and eventually stabilizes. This trend is closely related to the doping concentration, which is further discussed in Fig. 6b. Fig. 6b depicts the relationship between doping concentration and adsorption energy, where the *x*-axis represents the number of electrons in graphene. Positive values indicate an increase in electron number, while negative values indicate a decrease. It is evident that as the electron number in graphene increases, meaning as the N-type doping concentration increases, the adsorption energy also increases. Combining the results in Fig. 6a and b, it can be inferred that as the n-type doping concentration of graphene increases, the adsorption energy rises, relaxation time shortens, and the time required for gas molecules to reach saturation on the graphene surface becomes shorter. This conclusion is consistent with the findings shown in Fig. 5b.

3.4. Practical performance and reliability in air

Fig. 7 demonstrates the NO_2 sensing performance of the UV-regulated graphene-based sensor under laboratory air conditions (20–22 °C, RH 40%), aiming to confirm whether the ultrafast response observed in nitrogen-based tests persists in a more realistic ambient environment. Fig. 7a presents the

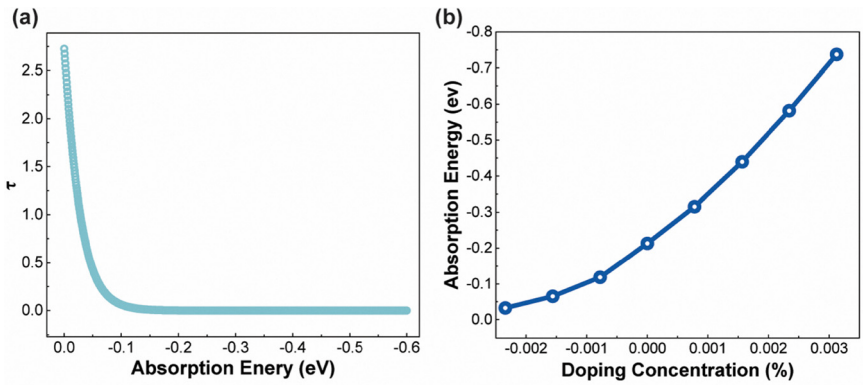

Fig. 6 (a) Calculated relationship between adsorption energy and relaxation time. (b) Calculated adsorption energy as a function of the electron number in graphene (n-type doping concentration), illustrating that stronger n-type doping leads to higher adsorption energy.

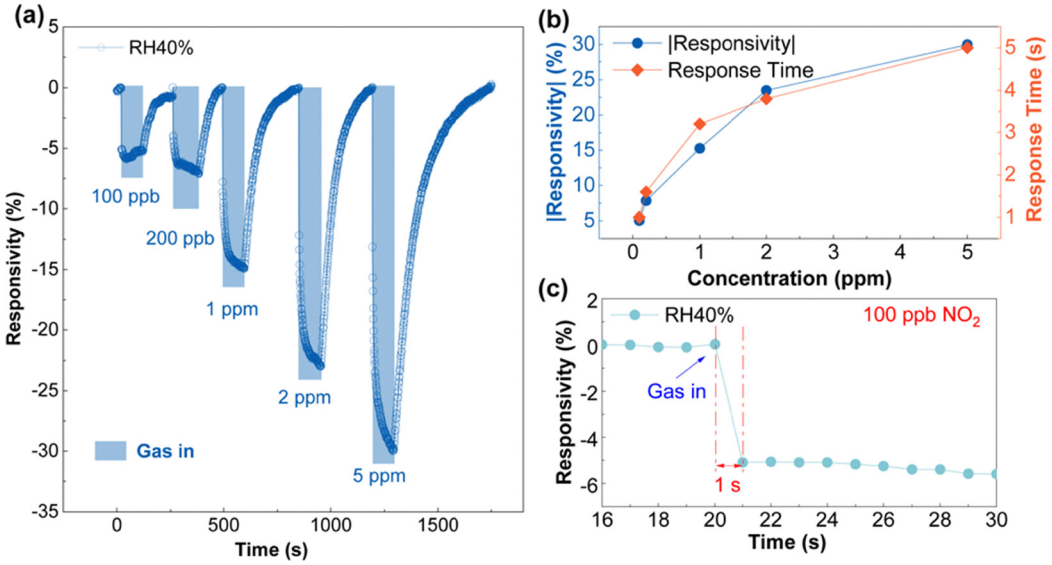

Fig. 7 NO_2 sensing performance of the graphene-based gas sensor under laboratory air conditions (20–22 °C, RH 40%) and UV illumination of 89.85 mW cm^{-2}: (a) dynamic response curves toward 100 ppb–5 ppm NO_2. (b) |Responsivity| and response time as a function of NO_2 concentration (note: the responsivity values are presented in absolute value form to clearly show the response trend). (c) Dynamic response curve of the sensor toward 100 ppb NO_2.

real-time response curves for 100 ppb, 200 ppb, 1 ppm, 2 ppm, and 5 ppm NO_2. The sensor exhibited a significant decrease in resistance upon exposure to NO_2, with responsivity progressively increasing as the NO_2 concentration rose. This indicates that the sensor possesses high sensitivity over a wide concentration range, accurately reflecting changes in NO_2 levels. Furthermore, the response curves displayed good reversibility, indicating that the sensor can effectively recover toward its baseline after NO_2 removal under 40% RH atmospheric conditions. Building on the observations from Fig. 7a and b shows the relationship between the responsivity and response time of the sensor with respect to NO_2 concentration. The responsivity increases monotonically with concentration and approaches saturation at higher concentrations (5 ppm). The response time increases with rising concentration but remains within 5 s overall, demonstrating the rapid response capability of the sensor under air conditions, which is highly significant for practical environmental monitoring. It is worth noting that the responsivity values are presented in absolute value form to clearly illustrate the trend in response magnitude, regardless of the sign of the resistance change. Complementing the results in Fig. 7a–c highlights the real-time response curve of the sensor to 100 ppb NO_2, showing an ultrafast transient response with a response time of only 1 s. The sensor sensitivity and rapid response to low NO_2 concentrations further validate its potential for detecting trace amounts of NO_2 in environmental monitoring applications. Table 1 summarizes the performance parameters of graphene-based NO_2 gas sensors reported in recent years. A comparison reveals that the sensor in this study exhibits a significant advantage in response time, achieving an ultrafast response of about 1 s even at low NO_2 concentrations of 100 ppb.

It is worth noting that, compared to the nitrogen environment, the sensor exhibited a reduced responsivity to the same concentration of NO_2 under ambient air conditions. This reduction can be qualitatively understood in terms of the preoccupation of active sites on the graphene surface by water and oxygen molecules in the air, which competes with NO_2 adsorption and reduces the number of available adsorption sites.

Although such competitive "site-blocking" lowers the overall response amplitude of the sensor, it also reduces the time

Table 1 Performance parameters of graphene-based NO_2 gas sensors reported in recent literature

Materials	Concentration	Responsivity	Response time	Ref.
RGO	500 ppb	88.76%	>10 min	36
RGO	5 ppm	36.7%	540 s	34
RGO	1 ppm	76	116 s	35
In_2O_3/RGO	10 ppb	3.79	4 min	54
In_2O_3/RGO	5 ppm	37.81%	3 min	55
S-RGO	200 ppb	6.1%	12 s	38
Ag NPs/S-RGO	500 ppb	1.49%	12 s	37
SnO_2 NPs/S-RGO	1 ppm	14.5%	40 s	39
Pd NPs-SnO_2 NPs/RGO	50 ppb	1.3	13s	40
ME	500 ppb	4%	500 s	56
EG	10 ppm	18.9%	15 min	14
EG	154 ppb	76.1%	>40 min	57
CVD-G	1 ppm	5%	100 s	26
CVD-G	100 ppb	4%	>30 min	24
CVD-G	1 ppm	6%	>10 min	30
CVD-G	1 ppm	1.41%	>10 min	27
PPy/CVD-G	100 ppb	7%	2 s	41
MoS_2/CVD-G	200 ppb	15%	6.5 s	58
CVD-G	100 ppb	6%	1 s	This Work[a]

[a] For this work, the response time at 100 ppb NO_2 in air is evaluated using the 90% response criterion so that the 1 s value reported here is directly comparable to the literature data in Table 1.S-RGO: sulfonated reduced graphene oxide; ME: mechanically exfoliated graphene: EG: epitaxial graphene; CVD-G: CVD graphene; PPy: polypyrrole.

required for NO_2 to reach a quasi-steady coverage within the fixed exposure window, so that the response time remains within a few seconds.

Therefore, despite the fact that graphene exhibits p-type conductivity under air conditions and the responsivity is lower than in nitrogen, the overall response speed remains largely unaffected, and the sensor is still capable of detecting NO_2 within a few seconds under UV illumination.

Together with the UV-induced elevation of the Fermi level and the enhanced charge-transfer kinetics discussed above, this provides a consistent qualitative explanation for the observed behavior of ''lower responsivity but maintained fast response'' under realistic air conditions.

Fig. 8 provides a broader evaluation of the sensor's operational stability in laboratory air by examining varying humidity conditions, multiple testing cycles, and long-term storage at 20–22 °C. Fig. 8a presents the dynamic response curves of the sensor under different RH levels (0%, 10%, 37%, 50%, 60%, and 75%) for 5 ppm NO_2. The results show that upon NO_2 exposure, the sensor resistance decreases, and the responsivity increases with rising humidity. The corresponding relationships between responsivity, response time, and RH are depicted in Fig. 8b. The responsivity increases significantly from 15% to 40% as humidity rises, but tends to stabilize as RH increases from 60% to 75%. This behavior is attributed to the physical adsorption of water molecules on the graphene surface at room temperature, which generates H^+ or H_3O^+ ions.[59,60] These ions react with NO_2^- adsorbed on the graphene surface to form nitric acid,[61] enhancing NO_2 molecule adsorption and increasing the responsivity. However, at RH levels above 60%, most adsorption sites are already saturated with water molecules. Further increases in humidity do not significantly enhance water molecule occupation, resulting in a stabilization of NO_2 adsorption and, consequently, the responsivity. Regarding response time, the sensor exhibits a response time of 2 s at 0% RH, which decreases to 1 s at 10% RH. As RH continues to increase, the response time remains stable at 1 s. This is because, in the presence of water molecules, a water film forms

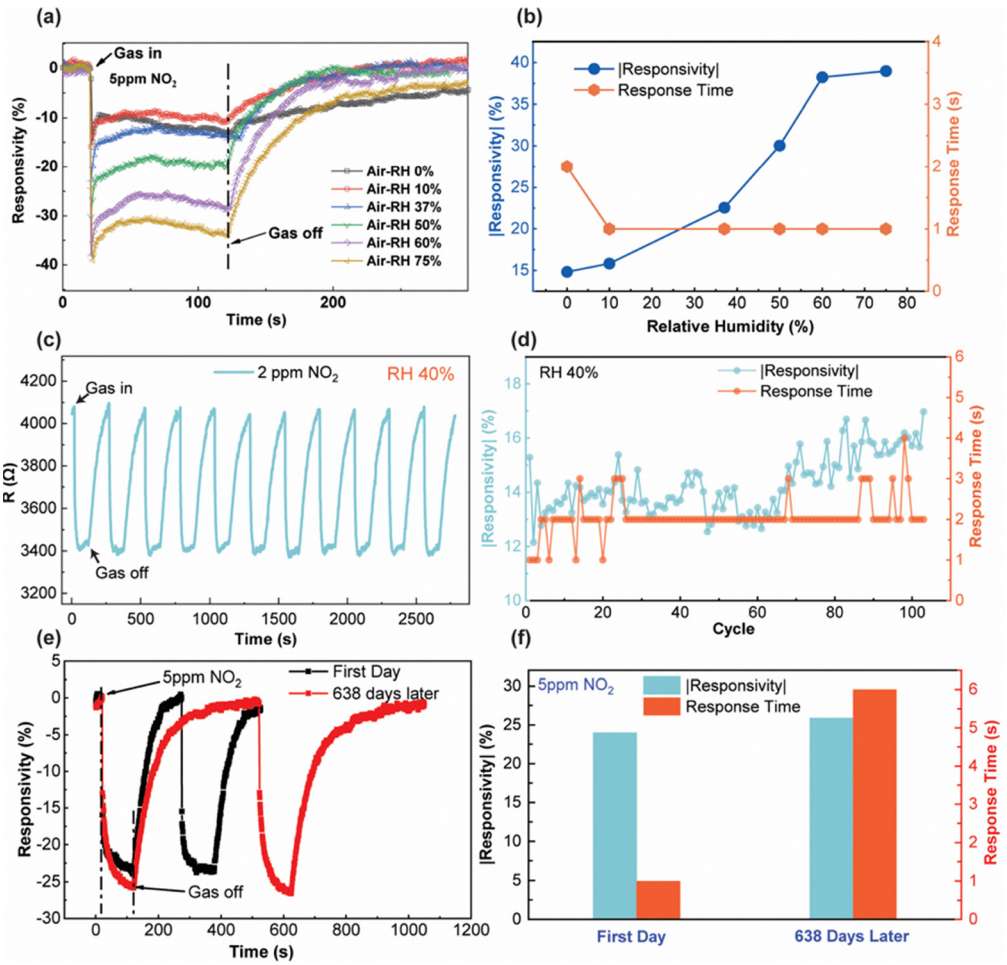

Fig. 8 NO_2 sensing performance of the graphene-based gas sensor under laboratory air conditions (20–22 °C) and UV illumination of 89.85 mW cm^{-2}: (a) dynamic response curves at different relative humidities (0–75% RH) for 5 ppm NO_2. (b) Corresponding |responsivity| and response time as a function of RH for 5 ppm NO_2. (c) Dynamic response characteristic curves for 11 consecutive tests at 2 ppm NO_2 (RH 40%). (d) |Responsivity| and response time over 100 consecutive tests at 2 ppm NO_2. (e) and (f) Comparison of response characteristics: initial test *vs.* after 638 days of storage. Responsivity in (b), (d), and (f) is plotted as the absolute value to clearly show the variation in response magnitude.

on the graphene surface, which can dissolve and accelerate the transport of NO_2 molecules, enabling faster adsorption on the sensor surface and reducing the response time. However, the transport capacity of the water film is limited, leading to a stabilization of the response time at 1 s as RH increases further. Overall, the sensor demonstrates only a weak influence of humidity on response time, maintaining rapid detection of NO_2 at RH levels up to 75%. Although responsivity is influenced by humidity variations, in practical applications, humidity sensors can be employed to calibrate the results, so that the sensor can rapidly and accurately detect NO_2 gas under varying humidity conditions.

Fig. 8c shows the dynamic resistance change response curves of the sensor under cyclic tests for 2 ppm NO_2 in an environment with RH 40%. Throughout the test, the resistance changes remain stable, demonstrating consistent sensor performance. This stability is further supported by the results shown in Fig. 8d, which presents the responsivity and response time during 100 consecutive tests for 2 ppm NO_2. The responsivity is initially in the range of 12%–15% for the first 60 cycles and then increased to 14%–17%, representing a change of approximately 15%. The response time remained under 4 seconds for most cycles, with the majority showing a response time of 2 s. These results demonstrate that the sensor maintained fast response times and responsivity deviations of less than 15% throughout 100 consecutive tests, highlighting its excellent repeatability and stability during continuous use. To further evaluate the long-term stability of the sensor, Fig. 8e and f compare the response characteristics of the sensor to 5 ppm NO_2 on the initial day and after 638 days of storage. During this period, the sensor was stored under ambient laboratory conditions without encapsulation or any special protection. After 638 days, the responsivity remained largely unchanged, while the response time increased from 1 s to 6 s. This moderate slowdown is likely related to trap-assisted interfacial relaxation. In graphene devices on insulating substrates, the resistance transient often contains a slow relaxation component associated with charge trapping/detrapping and interfacial polarization, which influences how fast the resistance reaches its new steady state. Such slow relaxation can become more pronounced after long-term storage, possibly associated with changes in trap occupancy and interfacial dipole configuration. The recovery time also extended but still allowed complete recovery. These findings indicate that the sensor retains useful and fast response characteristics even after long-term storage.

To evaluate the selectivity of the UV-regulated graphene sensor, we measured its response to several common interfering gases under the same operating conditions as the NO_2 tests. As summarized in Fig. 9, the sensor shows a pronounced response of about −15% to 1 ppm NO_2, whereas the responses to 1 ppm H_2S, 500 ppm NH_3, 500 ppm CO, 2.5% CH_4, 2.5% C_2H_4, 2.5% C_3H_8 and 100 ppm H_2 are all very small, remaining within ±2%. It is also worth noting that these interfering gases were tested at concentrations equal to or even much higher than that of NO_2. These results demonstrate that, under the chosen operating conditions, the sensor exhibits good selectivity toward NO_2 over these common interfering gases.

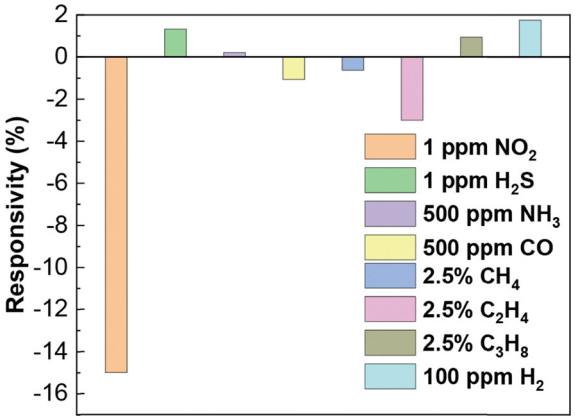

Fig. 9 Selectivity of the graphene-based gas sensor toward different gases at room temperature, showing the responsivity of the sensor to 1 ppm NO_2, 1 ppm H_2S, 500 ppm NH_3, 500 ppm CO, 2.5% CH_4, 2.5% C_2H_4, 2.5% C_3H_8, and 100 ppm H_2 under UV illumination of 89.85 mW cm^{-2} in air (20–22 °C).

Conclusions

In this study, we systematically investigated a UV-regulated graphene-based NO_2 gas sensor in both high-purity nitrogen (for mechanism exploration) and air (for practical performance validation). Specifically, the sensor exhibited rapid room-temperature response under air conditions, with response times below 5 s for NO_2 concentrations ranging from 0.1 to 5 ppm, and a response time of about 1 s at 100 ppb NO_2. This ultrafast detection is primarily attributed to the UV-induced elevation of graphene's Fermi level, enhancing adsorption energy and accelerating NO_2 adsorption/desorption processes. In air with relative humidity up to 75%, the sensor maintained reliable operation, and the responsivity variation over 100 consecutive tests was within 15%. Additionally, it retained its response characteristics even after 638 days of storage, underscoring its long-term durability. Complementary measurements in nitrogen helped isolate the intrinsic interaction between graphene and NO_2, further confirming the fundamental role of UV-enhanced charge-transfer mechanisms. In addition, selectivity tests showed that the sensor exhibits a strong response to NO_2 while producing negligible responses to other common gases, even at much higher concentrations. Overall, this study highlights how controlling graphene's electronic properties *via* UV illumination enables ultrafast, highly selective and stable NO_2 detection in realistic environments, offering a feasible method for rapid room-temperature sensing applications.

Author contributions

Wei Jin: methodology, investigation, data curation, carrying out experiments of photolithography, RIE and ALD, writing – original draft preparation. Cao Tang: the synthesis of CVD graphene, investigation, data curation. Hongyuan Zhao: theoretical simulation, data curation. Xue Xiao: data curation. Xin Qi: data curation. Xiangting Zhang: data curation. Hafiza Sana

Haider: data curation. Jianxiong Zhao: writing – review & editing. Yanqing Ma: writing – review & editing, supervision. Lei Ma: conceptualization, methodology, funding acquisition, supervision, writing – review & editing.

Conflicts of interest

The authors declare that they have no known competing financial interests or personal relationships that could have appeared to influence the work reported in this paper.

Data availability

All data supporting the findings of this study are available within the article and its supplementary information (SI). Supplementary information including reagents and materials, Raman spectrum, transfer characteristics, and theoretical simulations. See DOI: https://doi.org/10.1039/d5tc04343c.

Acknowledgements

This work was financially supported by the National Key R&D Program of China (No. 2022YFC3006303) and Tianjin Natural Science Foundation Project (No. 25JCZDJC01380). Also was supported by the Innovation fund of Haihe Laboratory of Low-dimensional Electronic Materials (25HHDWSS00005).

References

1 J. P. Singh, A. Sharma, M. Tomar and A. Chowdhuri, *J. Electron. Mater.*, 2024, **53**, 6688–6699.
2 B. Zhang, Z. Zhang, C. Wang, B. Zhang, S. Zhang, N. Luo, H. Bala and Y. Wang, *ACS Appl. Nano Mater.*, 2024, **7**, 28457–28465.
3 C. Wang, Y. Wang, Z. Yang and N. Hu, *Ceram. Int.*, 2021, **47**, 16367–16384.
4 G. L. Tan, D. Tang, X. M. Wang and X. T. Yin, *ACS Appl. Nano Mater.*, 2022, **5**, 12300–12319.
5 F. Schedin, A. K. Geim, S. V. Morozov, E. W. Hill, P. Blake, M. I. Katsnelson and K. S. Novoselov, *Nat. Mater.*, 2007, **6**, 652–655.
6 G. Ko, H. Y. Kim, J. Ahn, Y. M. Park, K. Y. Lee and J. Kim, *Curr. Appl. Phys.*, 2010, **10**, 1002–1004.
7 H. J. Yoon, D. H. Jun, J. H. Yang, Z. Zhou, S. S. Yang and M. M. C. Cheng, *Sens. Actuators, B*, 2011, **157**, 310–313.
8 S. Rumyantsev, G. Liu, M. S. Shur, R. A. Potyrailo and A. A. Balandin, *Nano Lett.*, 2012, **12**, 2294–2298.
9 Z. Zhang, X. Zou, L. Xu, L. Liao, W. Liu, J. Ho, X. Xiao, C. Jiang and J. Li, *Nanoscale*, 2015, **7**, 10078–10084.
10 M. W. K. Nomani, R. Shishir, M. Qazi, D. Diwan, V. B. Shields, M. G. Spencer, G. S. Tompa, N. M. Sbrockey and G. Koley, *Sens. Actuators, B*, 2010, **150**, 301–307.
11 R. Pearce, T. Iakimov, M. Andersson, L. Hultman, A. L. Spetz and R. Yakimova, *Sens. Actuators, B*, 2011, **155**, 451–455.
12 I. Iezhokin, P. Offermans, S. H. Brongersma, A. J. M. Giesbers and C. F. J. Flipse, *Appl. Phys. Lett.*, 2013, **103**, 053514.
13 S. Novikov, N. Lebedeva, A. Satrapinski, J. Walden, V. Davydov and A. Lebedev, *Sens. Actuators, B*, 2016, **236**, 1054–1060.
14 P. D. Kaushik, I. G. Ivanov, P. C. Lin, G. Kaur, J. Eriksson, G. B. V. S. Lakshmi, D. K. Avasthi, V. Gupta, A. Aziz, A. M. Siddiqui, M. Syväjärvi and G. R. Yazdi, *Appl. Surf. Sci.*, 2017, **403**, 707–716.
15 S. S. Niavol, M. Budde, A. Papadogianni, M. Heilmann, H. M. Moghaddam, C. M. Aldao, G. Ligorio, E. J. W. List-Kratochvil, J. M. J. Lopes, N. Barsan, O. Bierwagen and F. Schipani, *Sens. Actuators, B*, 2020, **325**, 128797.
16 J. T. Robinson, F. K. Perkins, E. S. Snow, Z. Wei and P. E. Sheehan, *Nano Lett.*, 2008, **8**, 3137–3140.
17 J. D. Fowler, M. J. Allen, V. C. Tung and B. H. Weiller, *ACS Nano*, 2009, **3**, 301–306.
18 T. H. Han, Y. K. Huang, A. T. Tan, V. P. Dravid and J. Huang, *J. Am. Chem. Soc.*, 2011, **133**, 15264–15267.
19 X. M. Geng, W. W. Li, Y. F. Guo, J. Z. Rong, Y. P. Gong, L. Q. Wu, X. M. Zhang, P. Li, J. B. Xu, G. S. Cheng, M. T. Sun and L. W. Liu, *ACS Nano*, 2011, **5**, 6955–6961.
20 A. Lipatov, A. Varezhnikov, P. Wilson, V. Sysoev, A. Kolmakov and A. Sinitskii, *Nanoscale*, 2013, **5**, 5426–5434.
21 S. Borini, R. White, D. Wei, M. Astley, S. Haque, E. Spigone, N. Harris, J. Kivioja and T. Ryhanen, *ACS Nano*, 2013, **7**, 11166–11173.
22 F. Rasch, V. Postica, F. Schütt, Y. K. Mishra, A. S. Nia, M. R. Lohe, X. Feng, R. Adelung and O. Lupan, *Sens. Actuators, B*, 2020, **320**, 128363.
23 W. Wu, Z. Liu, L. A. Jauregui, Q. Yu, R. Pillai, H. Cao, J. Bao, Y. P. Chen and S. S. Pei, *Sens. Actuators, B*, 2010, **150**, 296–300.
24 F. Yavari, E. Castillo, H. Gullapalli, P. M. Ajayan and N. Koratkar, *Appl. Phys. Lett.*, 2012, **100**, 203120.
25 H. Choi, J. S. Choi, J. S. Kim, J. H. Choe, K. H. Chung, J. W. Shin, J. T. Kim, D. H. Youn, K. C. Kim, J. I. Lee, S. Y. Choi, P. Kim, C. G. Choi and Y. J. Yu, *Small*, 2014, **10**, 3685–3691.
26 Y. H. Kim, S. J. Kim, Y. J. Kim, Y. S. Shim, S. Y. Kim, B. H. Hong and H. W. Jang, *ACS Nano*, 2015, **9**, 10453–10460.
27 Y. Seekaew, D. Phokharatkul, A. Wisitsoraat and C. Wongchoosuk, *Appl. Surf. Sci.*, 2017, **404**, 357–363.
28 X. Yang and M. Yan, *Nano Res.*, 2020, **13**, 599–610.
29 C. Lee, J. Ahn, K. B. Lee, D. Kim and J. Kim, *Thin Solid Films*, 2012, **520**, 5459–5462.
30 H. Choi, H. Y. Jeong, D. S. Lee, C. G. Choi and S. Y. Choi, *Carbon Lett.*, 2013, **14**, 186–189.
31 A. Cagliani, D. M. A. Mackenzie, L. K. Tschammer, F. Pizzocchero, K. Almdal and P. Bøggild, *Nano Res.*, 2014, **7**, 743–754.
32 J. Wu, S. Feng, X. Wei, J. Shen, W. Lu, H. Shi, K. Tao, S. Lu, T. Sun, L. Yu, C. Du, J. Miao and L. K. Norford, *Adv. Funct. Mater.*, 2016, **26**, 7462–7469.

33 V. Strong, S. Dubin, M. F. El-Kady, A. Lech, Y. Wang, B. H. Weiller and R. B. Kaner, *ACS Nano*, 2012, **6**, 1395–1403.
34 T. Han, S. Gao, Z. Wang, T. Fei, S. Liu and T. Zhang, *J. Alloys Compd.*, 2019, **801**, 142–150.
35 J. Wu, Z. Li, X. Xie, K. Tao, C. Liu, K. A. Khor, J. Miao and L. K. Norford, *J. Mater. Chem. A*, 2018, **6**, 478–488.
36 H. Peng, F. Li, Z. Hua, K. Yang, F. Yin and W. Yuan, *Sens. Actuators, B*, 2018, **275**, 78–85.
37 L. Huang, Z. Wang, J. Zhang, J. Pu, Y. Lin, S. Xu, L. Shen, Q. Chen and W. Shi, *ACS Appl. Mater. Interfaces*, 2014, **6**, 7426–7433.
38 J. Wu, K. Tao, Y. Guo, Z. Li, X. Wang, Z. Luo, S. Feng, C. Du, D. Chen, J. Miao and L. K. Norford, *Adv. Sci.*, 2017, **4**, 1600319.
39 S. Liu, Z. Wang, Y. Zhang, J. Li and T. Zhang, *Sens. Actuators, B*, 2016, **228**, 134–143.
40 Z. Wang, T. Zhang, C. Zhao, T. Han, T. Fei, S. Liu and G. Lu, *J. Colloid Interface Sci.*, 2018, **514**, 599–608.
41 T. Yoon, J. Jun, D. Y. Kim, S. Pourasad, T. J. Shin, S. U. Yu, W. Na, J. Jang and K. S. Kim, *J. Mater. Chem. A*, 2018, **6**, 2257–2263.
42 Z. Yan, J. Lin, Z. W. Peng, Z. Z. Sun, Y. Zhu, L. Li, C. S. Xiang, E. L. Samuel, C. Kittrell and J. M. Tour, *ACS Nano*, 2012, **6**, 9110–9117.
43 H. Wang, G. Wang, P. Bao, S. Yang, W. Zhu, X. Xie and W. J. Zhang, *J. Am. Chem. Soc.*, 2012, **134**, 3627–3630.
44 A. C. Ferrari, J. C. Meyer, V. Scardaci, C. Casiraghi, M. Lazzeri, F. Mauri, S. Piscanec, D. Jiang, K. S. Novoselov, S. Roth and A. K. Geim, *Phys. Rev. Lett.*, 2006, **97**, 187401.
45 Y. Hao, Y. Wang, L. Wang, Z. Ni, Z. Wang, R. Wang, C. K. Koo, Z. Shen and J. T. Thong, *Small*, 2010, **6**, 195–200.
46 L. G. Cançado, A. Jorio, E. H. M. Ferreira, F. Stavale, C. A. Achete, R. B. Capaz, M. V. O. Moutinho, A. Lombardo, T. S. Kulmala and A. C. Ferrari, *Nano Lett.*, 2011, **11**, 3190–3196.
47 T. Xie, Q. Wang, R. M. Wallace and C. Gong, *Appl. Phys. Lett.*, 2021, **119**, 013104.
48 B. Dörling, J. D. Ryan, J. D. Craddock, A. Sorrentino, A. E. Basaty, A. Gomez, M. Garriga, E. Pereiro, J. E. Anthony, M. C. Weisenberger, A. R. Goñi, C. Müller and M. Campoy-Quiles, *Adv. Mater.*, 2016, **28**, 2782–2789.
49 C. M. Yang, T. C. Chen, Y. C. Yang, M. Meyyappan and C. S. Lai, *Sens. Actuators, B*, 2017, **253**, 77–84.
50 P. Sun, M. Zhu, K. Wang, M. Zhong, J. Wei, D. Wu, Y. Cheng and H. Zhu, *Appl. Phys. Lett.*, 2012, **101**, 053107.
51 H. E. Romero, N. Shen, P. Joshi, H. R. Gutierrez, S. A. Tadigadapa, J. O. Sofo and P. C. Eklund, *ACS Nano*, 2008, **2**, 2037–2044.
52 Z. Luo, N. J. Pinto, Y. Davila and A. T. C. Johnson, *Appl. Phys. Lett.*, 2012, **100**, 253108.
53 Y. J. Lin and J. J. Zeng, *Appl. Phys. Lett.*, 2013, **102**, 183120.
54 J. Liu, S. Li, B. Zhang, Y. Wang, Y. Gao, X. Liang, Y. Wang and G. Lu, *J. Colloid Interface Sci.*, 2017, **504**, 206–213.
55 W. Yang, P. Wan, X. Zhou, J. Hu, Y. Guan and L. Feng, *ACS Appl. Mater. Interfaces*, 2014, **6**, 21093–21100.
56 A. Reina, X. T. Jia, J. Ho, D. Nezich, H. Son, V. Bulovic, M. S. Dresselhaus and J. Kong, *Nano Lett.*, 2009, **9**, 30–35.
57 C. Melios, V. Panchal, K. Edmonds, A. Lartsev, R. Yakimova and O. Kazakova, *ACS Sens.*, 2018, **3**, 1666–1674.
58 H. S. Hong, N. H. Phuong, N. T. Huong, N. H. Nam and N. T. Hue, *Appl. Surf. Sci.*, 2019, **492**, 449–454.
59 F. Pourfayaz, Y. Mortazavi, A. Khodadadi and S. Ajami, *Sens. Actuators, B*, 2008, **130**, 625–629.
60 X. Wang, Y. Chen, H. Qin, L. Li, C. Shi, L. Liu and J. Hu, *Phys. Chem. Chem. Phys.*, 2015, **17**, 13733–13742.
61 W. Yan, M. A. Worsley, T. Pham, A. Zettl, C. Carraro and R. Maboudian, *Appl. Surf. Sci.*, 2018, **450**, 372–379.

